Identification of common minerals using stoichiometric calibration method for dual-energy CT.

M. Martini[1], P. Francus[1,3], L. Di Schiavi Trotta[2], P. Després[2].

[1]Centre Eau Terre Environnement, Institut National de la Recherche Scientifique, Québec, Canada

[2]Department of Physics, Physical Engineering and Optics, Université Laval, Québec, Canada

[3]GEOTOP – Research Centre on the Dynamics of the Earth System, Montréal, Québec, H2X 3Y7, Canada

Corresponding author: Margherita Martini (margherita.martini@ete.inrs.ca)

Key Points:

- Dense materials as minerals are scanned with medical computed tomography.
- A Dual-energy stoichiometric method is applied for the first time to characterize geological samples.
- The most important and common minerals are correctly identified.

Key Words:

Geoscience, X-rays, medical CT, effective atomic number, electron density, minerals characterization

Index Terms:

6900 RADIO SCIENCE
6982 Tomography and imaging (7270, 8180)

Abstract

Medical X-ray computed tomography (CT) can be used to rapidly and non-destructively characterize structure and density variations of geological specimens. More information about the nature of samples (electron density and elemental composition) can be retrieved using multi-spectral approaches. This paper explores one of them, a stoichiometric calibration method for dual-energy imaging, to identify the most common minerals. A set of 18 calibrating materials was selected to cover a range of variability in effective atomic number (Z_{eff}) and electron density (ρ_e) encountered in geological specimens.

The validation of this calibration was performed analyzing 23 common minerals by mapping their respective Z_{eff} and ρ_e in order to identify the one with the closest properties. This study shows that the stoichiometric method correctly identifies the most important and common minerals (quartz, calcite, dolomite) that are usually not distinguishable using a single energy imaging method, although all the 23 studied minerals were not correctly determined. We show that this method previously elaborated for medical purposes is also efficient in earth science.

Plain Language Summary

Medical CT-scanners measure the attenuation of X-rays that go through a sample allowing the non-destructive 3D internal structure visualization of a wide range of samples. The attenuation depends on the interaction between incident beam and sample local density and chemical composition. By scanning specimens using two different energies, it is possible to track the attenuation changes (grey level) according to the X-ray spectra, and to use this difference to identify the samples. This paper tests the applicability of one method developed by medical physicists for biological tissues on 23 common minerals. While all minerals are not correctly identified, this method recognizes the most important and common ones in geology (quartz, calcite, dolomite).

1. Introduction

X-ray computed tomography (CT) is a non-destructive technique allowing the visualization of sample internal structure. A medical CT scanner consists in an X-ray source and a detector, which face each other and rotate around the sample. Bi-dimensional radiographic projections are acquired at various angles from 0° to 360° and then processed by a mathematical algorithm (i.e., image reconstruction) in order to obtain a 3D visualization of the object. Different types of image reconstructions exist, including the widely used filtered backprojection that requires little computational resources but produces less qualitatively accurate images, and iterative reconstruction, based on time consuming and numerically intensive algorithm but providing better images quality (Bushberg et al., 2012).

The images are displayed in a gray scale related to the X-ray attenuation by the sample materials (Rizescu et al., 2001).

Initially, this technology was developed for medical imaging, but its potential for other domains was rapidly understood (Mees et al., 2003).

This paper explores a specific CT methodology, called dual-energy CT scanning (DECT), elaborated for the first time in the seventies by Alvarez et al. (1976). The technique consists in imaging objects with two different X-ray spectra and in combining the results to achieve various objectives, including one allowing the discrimination and identification of materials based on their density and elemental composition. From a physical perspective, DECT exploits the energy dependence of photoelectric absorption and Compton scattering components of total attenuation (Duchesne et al., 2009). The method of Alvarez et al. (1976) acts on the 2D radiographic projections and is therefore called a pre-reconstruction one.

During the same year, Rutherford et al. (1976) published another DECT methodology which, on the contrary, is post-reconstruction, meaning the correction is performed on the reconstructed data. This method is more sensitive to beam hardening artifacts, caused by the presence of highly attenuating materials in the sample (Remysen et al., 2006). Several variations of the post-reconstruction approach have been developed afterwards, in order to improve sample characterization (e.g., Jackson et al. (1981), Vinegar et al. (1987), Torikoshi et al. (2003), Tsunoo et al. (2004), Bazalova et al. (2008)).

One of the first DECT post-reconstruction applications in geology field was made by Van Geet et al. (2000), who adapted the mathematical formulas previously elaborated by Coenen et al. (1994) in order to quantify the electron density (ρ_e) and the effective atomic number (Z_{eff}) of reservoir rocks, properties originally analyzed only by destructive techniques (Alves et al., 2015). Then, geologists continued to improve this post-reconstruction dual-energy method *ad hoc* for earth's science (Rizescu et al., 2001, Duliu et al., 2003), sometimes building home-made CT scanner (Iovea et al., 2006) and better distinguishing similar minerals and rocks (Remeysen et al., 2008, Iovea et al., 2009).

Later, Paziresh et al. (2016) applied the method of Alvarez et al. (1976) on geological samples adopting a protocol used for medical purposes. DECT techniques typically require the knowledge of the incident X-ray beam spectrum, a feature that is not always easy to calculate or to measure (Remysen et al., 2006). Therefore, DECT methods that not require spectral information were developed and applied mostly to the field of medical imaging (e.g., Landry et al. (2013) and Bourque et al. (2014)). While several authorsexplored the use of DECT on geological samples

(e.g.,Siddiqui et al. (2004), Alves et al. (2015), Jussiani et al. (2015), Victor et al. (2017)), they were mainly using micro-CT instruments for which the incident spectrum was easily available, focussing on artificial dense objects (metal bars) (Rezvan et al., 2011), or requiring intensive computation (Victor et al., 2017). This paper is the first to explore the use of polynomial DECT protocol to identify natural mineral samples because it has two main advantages: it can be easily be applied on medical CT images for which the spectral information of the incident X-ray is not easy to obtain or to measure, and it is computationally light.

Materials and Methods

1.1. CT-scan instrument

The instrument used in this paper is a Siemens Somatom Definition AS+128 located at the *Institut national de la recherche scientifique, Centre Eau Terre Environment*, Québec City, Canada. In this configuration the gantry moves along the examination table where the samples are placed (figure 1) (Brunelle et al., 2016).

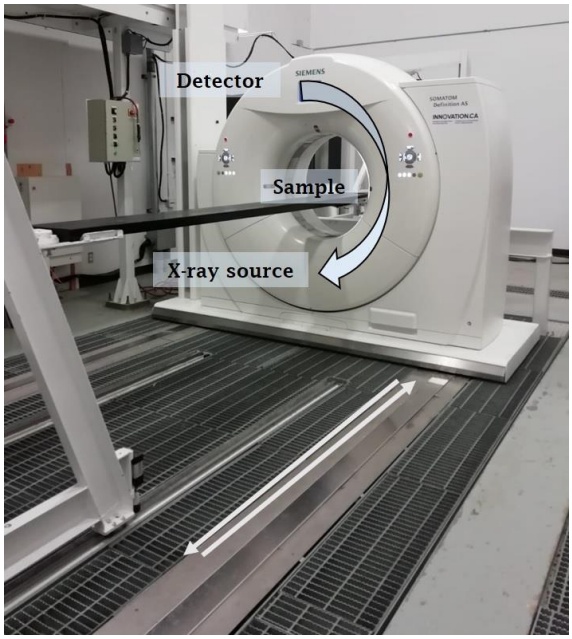

Figure 1: Siemens Somatom Definition AS+128 located at the Institut national de la recherche scientifique, Centre Eau Terre Environnement, Québec City, Canada. X-ray source and detector face each other in the gantry and rotate around the sample. The scanner moves on rails (white arrows).

The X-ray tube can be operated at potentials between 70 keV and 140 keV and the 64-row detector is from the Stellar^{Infinity} generation. Images were acquired in spiral mode with a pitch factor of 0.55, at 70 and 140 keV, 495 mA current and a beam collimation of 12 mm. Here, the reconstruction was performed with the ADMIRE suite, belonging to the category of statistical iterative reconstruction methods (Gordic et al., 2014). Reconstructed images are 512 x 512 pixels, covering a field of view of 50 mm x 50 mm wide (voxels of 97 µm along the axis). Pixel values depend on the object attenuation coefficient according to Beer's law (Cnudde et al., 2013), and expressed in Hounsfield units

(*HU*), a relative scale tied to the attenuation of materials (conventionally water has *HU*=0 and air *HU*=-1000), varying from -1024 to +3071 *HU* (normal scale), providing 4096 levels of grey (Brunelle et al., 2016). The CT-scale can be extended by scaling down the *HU* value by a factor of 10, expanding the possible values between -10240 and 30710 *HU*, a feature useful for very dense samples (Coolens et al., 2003). The reconstruction filter used was the D45s specifically designed by Siemens for dual-energy measurements and providing a balance between the preservation of spatial resolution and noise reduction.

1.2. Stoichiometric method

The stoichiometric method developed by Bourque et al. (Bourque et al., 2014) is a dual-energy CT protocol aiming at identifying the nature of biological tissues for medical purposes. It was based on the work of Schneider et al. (1996), a calibration elaborated for single energy CT, and Bourque et al. applied it to DECT, in order to facilitate the determination of effective atomic number (Z_{eff}) and electron density (ρ_e).

The theoretical effective atomic number Z_{eff} of samples is calculated with the following equation:

$$Z_{eff} = \sqrt[\beta]{\sum_i^N f_i Z_i^\beta} \quad (1)$$

where f_i is the fractional mass of element Z_i. As the literature reports, the exponent β can vary between 2.94 and 3.8 (Spiers et al., 1946, Bonnin et al., 2014) and it is a function of photon energy, sample materials and system specifics (Landry et al., 2013, Alves et al., 2015, Azevedo et al., 2016).

Then, the theoretical electron density ρ_e, expressed in number of electrons per unit volume (electron·cm^{-3}), is calculated as:

$$\rho_e = \sum_{i=1}^N \frac{Z_i}{A_i} \rho \quad (2)$$

where A_i is the atomic mass of the element Z_i and ρ is the material mass density (g·cm^{-3}) (Manohara et al., 2008, Azevedo et al., 2016).

The materials linear attenuation coefficient is calculated converting back CT measurements (*HU* values) as (Boespflug et al., 1995, Watanabe et al., 1999):

$$\mu = \frac{\mu_{sample}}{\mu_{water}} = \left(\frac{HU}{1000}\right) + 1 \quad (3)$$

Two different calibration procedures are necessary: the first one relates to the effective atomic number and the second one to the electron density.

First, the two linear attenuation values, measured at low and high energy (equation 3), and the calculated Z_{eff} (equation 1) of the basis set of samples are plotted to estimate the best relationship. In our case a second-order polynomial (equation 4) data-driven empirical model was used to set the *a*, *b* and *c* coefficients of the Z_{eff} calibration.

$$Z_{eff} = a + b \cdot \left(\frac{\mu_{low}}{\mu_{high}}\right) + c \cdot \left(\frac{\mu_{low}}{\mu_{high}}\right)^2 \quad (4)$$

It is then possible to achieve the ρ_e calibration (finding another set of coefficients) plotting the ratio between measured μ and ρ_e (equation 2), normalized by water electron density ($\rho_{e\ water} = 3.34 \cdot 10^{23}$) and Z_{eff} determined in equation 4:

$$\frac{\mu_{low\ or\ high}}{\rho_e / \rho_{e\ water}} = d + e \cdot Z_{eff} + f \cdot Z_{eff}^2 \quad (5)$$

Again, the data-driven empirical model is a second-order polynomial. The μ value can equally be those obtained low or high energy; it is also possible to use both equations to calculate ρ_e and average the outcomes.

2. Results

2.1. Calibration

The calibration procedure consists in scanning a set of materials with a known chemical composition (their Z_{eff} and ρ_e are calculated using the equations 1 and 2) in order to determine the unknown coefficients of equations 4 and 5.

A set of 18 calibration materials covering the range of Z_{eff} and ρ_e encountered in geological specimens (figure 2) was selected: common geological minerals (halite, crystalline quartz, pyrite, fluorite, albite) completed by Sodium Iodide (NaI) solutions at different concentrations, an aluminum and a titanium bar. The first ones are natural samples, so they do not have a precise chemical composition and always contain impurities, but their presence is important for the subsequent validation, being of the same nature as investigated samples (Stamm et al., 1974). Details about these calibration materials are available in table S1 in *Dataverse* repository (see section 6).

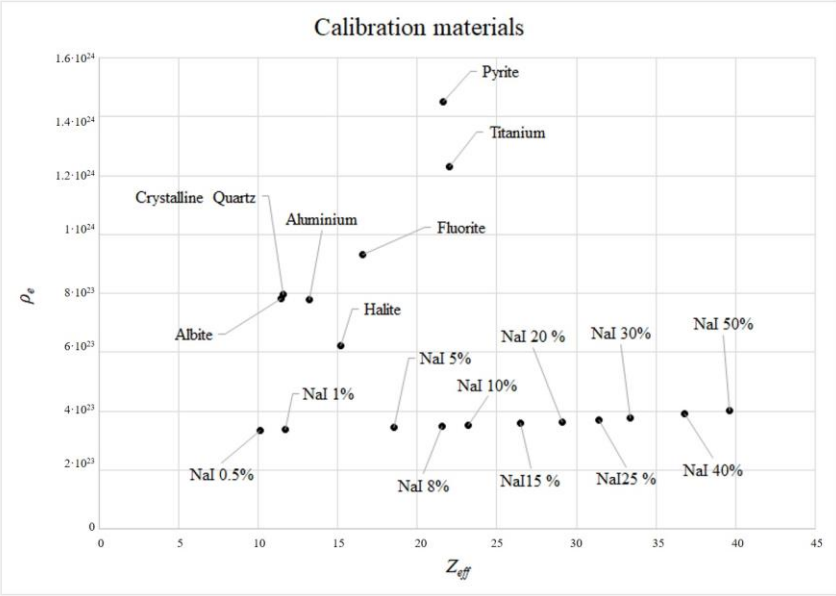

Figure 2: Electronic density and effective atomic number theoretical value distribution of calibration samples.

As anticipated, the best possible β exponent (equation 1) varies between 2.94 and 3.8 (Bonnin et al., 2014) depending on the material, the instrument and the energy considered. Our choice is based on the behaviour of determination coefficient (R^2) as function of β in the fitting of equation 4; figure 3 shows the best value in the possible range is 2.94.

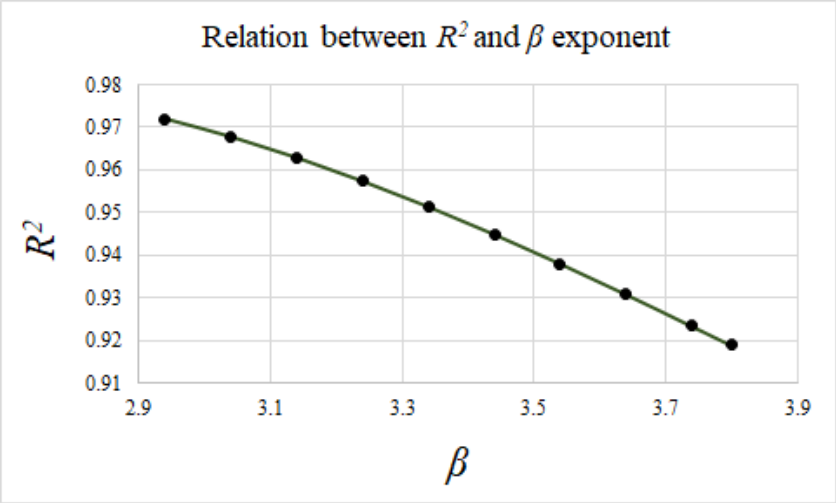

Figure 3: R^2 values against possible β of equation 1.

The effective atomic number calibration, following equation 4 to find *a*, *b* and *c* coefficients, is performed by plotting the Z_{eff} and μ_{low}/μ_{high} values of basis samples (figure 4); this fit presents R^2 = 0.97.

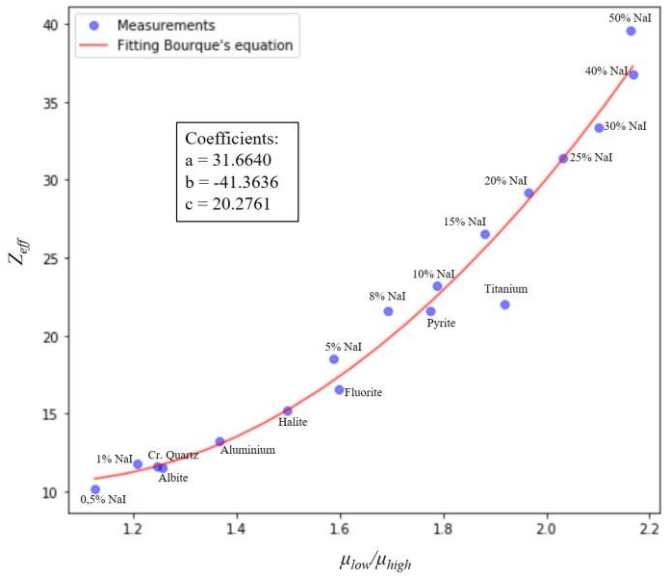

Figure 4: coefficients related to equation 4 and calibration curve with μ_{low}/μ_{high} as function of Z_{eff}.

Then, the electron density calibration, related to equation 5 aiming to obtain *d*, *e* and *f* coefficients, is shown in figure 5. As already mentioned, we can freely choose to use μ_{low} or μ_{high} in this model. We opted for μ_{low} obtained at 70 keV because the correlation was stronger (R^2= 0.98) compared to the one obtained at 140 keV (R^2= 0.96).

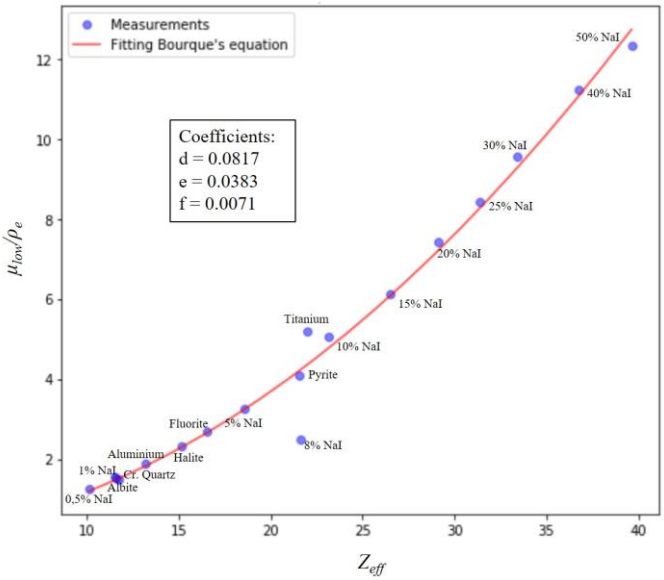

Figure 5: coefficients related to equation 5 and calibration curve with Z_{eff} as function of $\mu_{low}/(\rho_e/\rho_{e\ water})$.

2.2. Validation

A set of 23 relatively common minerals were used for the validation of the stoichiometric method (Table 1, column 1). Samples were about the same size as the ones of the calibration set (≃ 3 cm x 3 cm), and selected to ensure they cover a wide range of effective atomic number and electronic density. Their theoretical values of Z_{eff} and ρ_e have been calculated using equations 1 and 2 (Table 1, columns 3 and 4) starting from their theoretical chemical composition (Table 1, column 2).

Using the same acquisition conditions of the calibration step (equation 4) the Z_{eff} model and the measured linear attenuation coefficients μ (equation 3) at low and high energy (details are available in table S2, *Dataverse* repository, see section 6), we calculate the minerals Z_{eff} values (Table 1, column 5). Then, the relative difference between these measured values of Z_{eff} and the theoretical ones is shown in column 6 (Table1).

Successively and always using the same acquisition conditions, equation 5, the ρ_e model and the measured linear attenuation coefficients μ acquired at low energy, we calculate the minerals ρ_e (Table 1, column 7). Again, the relative difference between this measured values of ρ_e and the theoretical ones is shown in column 8 (table1).

(1)	(2)	(3)	(4)	(5)	(6)	(7)	(8)
Mineral	**Chemical composition**	**Theoretical Z_{eff}**	**Theoretical ρ_e ($e^- \cdot cm^{-3}$)**	**Measured Z_{eff}**	**% difference between theoretical and measured Z_{eff} values**	**Measured ρ_e**	**% difference between theoretical and measured ρ_e values**
Albite	$NaAlSi_3O_8$	11.472	$7.82 \cdot 10^{23}$	11.743	2.4 %	$7.81 \cdot 10^{23}$	0.1 %
Almandine	$Fe_3^{2+}Al_2Si_3O_{12}$	18.655	$1.23 \cdot 10^{24}$	20.514	9.9 %	$9.44 \cdot 10^{23}$	2.2 %
Andesine	$(Ca,Na)(Al,Si)_4O_8$	13.249	$7.97 \cdot 10^{23}$	12.599	3.1 %	$8.32 \cdot 10^{23}$	4.3 %
Ankerite	$Ca(Fe^{2+},Mg,Mn)(CO_3)_2$	16.989	$9.05 \cdot 10^{23}$	15.094	11.2 %	$7.29 \cdot 10^{23}$	19.4 %
Anorthite	$CaAl_2Si_2O_8$	13.206	$8.21 \cdot 10^{23}$	12.778	3.2 %	$8.27 \cdot 10^{23}$	0.6 %
Augite	$(Ca,Mg,Fe^{2+},Fe^{3+},Ti,Al)_2(Si,Al)_2O_6$	14.849	$1.01 \cdot 10^{24}$	15.589	4.9 %	$9.58 \cdot 10^{23}$	5.6 %
Biotite	$K(Mg,Fe^{2+})_3$	14.046	$9.26 \cdot 10^{23}$	13.741	2.2 %	$7.7 \cdot 10^{23}$	16.1 %
Bytownite	$(Ca,Na)[Al(Al,Si)Si_2O_8]$	12.961	$8.09 \cdot 10^{23}$	11.953	7.8 %	$8.13 \cdot 10^{23}$	0.4 %
Calcite	$CaCO_3$	15.079	$8.15 \cdot 10^{23}$	15.398	2.1 %	$7.96 \cdot 10^{23}$	2.3 %
Chalcopyrite	$CuFeS_2$	24.568	$1.20 \cdot 10^{24}$	22.741	7.4 %	$9.55 \cdot 10^{23}$	20.4 %
Diopside	$CaMgSi_2O_6$	13.729	$1.02 \cdot 10^{24}$	13.971	1.1 %	$9.59 \cdot 10^{23}$	6.1 %
Dolomite	$CaMg(CO_3)_2$	13.057	$8.53 \cdot 10^{23}$	13.101	0.3 %	$8.46 \cdot 10^{23}$	0.9 %
Gypsum	$CaSO_4 \cdot 2H_2O$	14.109	$7.11 \cdot 10^{23}$	14.246	0.9 %	$7.13 \cdot 10^{23}$	0.2 %
Hematite	Fe_2O_3	22.962	$1.52 \cdot 10^{24}$	17.882	22.1 %	$1.73 \cdot 10^{24}$	13.9 %
Ilmenite	$FeTiO_3$	21.327	$1.37 \cdot 10^{24}$	18.331	14.1 %	$1.40 \cdot 10^{24}$	2.4 %
Labradorite	$(Ca,Na)(Si,Al)_4O_8$	16.608	$8.06 \cdot 10^{23}$	12.558	0.4 %	$8.26 \cdot 10^{23}$	2.5 %
Magnetite	Fe_3O_4	23.231	$1.47 \cdot 10^{24}$	20.773	10.6 %	$8.57 \cdot 10^{23}$	41.9 %
Microcline	$KAlSi_3O_8$	13.018	$7.64 \cdot 10^{23}$	12.558	3.5 %	$7.95 \cdot 10^{23}$	3.9 %
Muscovite	$KAl_2(Si_3Al)O_{10}(OH,F)_2$	12.403	$8.46 \cdot 10^{23}$	12.999	4.8 %	$8.06 \cdot 10^{23}$	4.7 %
Olivine	$(Mg,Fe)_2SiO_4$	15.215	$9.80 \cdot 10^{23}$	12.701	16.5 %	$9.60 \cdot 10^{23}$	2.1 %
Phlogopite	$KMg_3(Si_3Al)O_{10}(F,OH)_2$	12.278	$8.46 \cdot 10^{23}$	14.769	20.3 %	$5.43 \cdot 10^{23}$	35.7 %
Quartz	SiO_2	11.561	$7.97 \cdot 10^{23}$	11.632	0.6 %	$8.11 \cdot 10^{23}$	1.7 %
Talc	$Mg_3Si_4O_{10}(OH)_2$	11.154	$8.30 \cdot 10^{23}$	11.587	3.9 %	$8.52 \cdot 10^{23}$	2.7 %

Table 1: validation minerals with their theoretical chemical composition and theoretical Z_{eff} and ρ_e calculated using equation 1 and 2. Then, Z_{eff} and ρ_e calculated using stoichiometric method and their relative difference (in %) with the theoretical values.

2.3. Mineral identification

The next step is to develop a tool to identify unknown minerals using Z_{eff} and ρ_e values measured by the dual-energy stoichiometric method. An *ad hoc* library of 69 common minerals (chosen from the database http://webmineral.com/, accessed Oct. 2020) was built using Python 3.7 as programming language (*CommonMinerals_database.py* in *Dataverse* repository, see section 6) mapping them to their respective Z_{eff} and ρ_e (theoretically properties calculated by equations 1 and 2).

Z_{eff} and ρ_e values differ by two orders of magnitude, thus they are normalized using the feature scaling method (Youn et al., 2009):

$$x' = \frac{x - \min(x)}{\max(x) - \min(x)}$$

Where x is the original value and x' is the normalized value. Then, another Python routine (*Minerals_Identification.py* in *Dataverse* repository, see section 6) searches this library to find the minerals with the shortest Euclidean distance to these theoretical properties, and provides a list of minerals with increasing Euclidean distance.

Table 2 shows the three closest minerals found using the searching program for each validation set of samples from table 1.

Mineral Specimen	1st	2nd	3rd	
Albite	**Albite**	Anorthoclase	Oligoclase	
Almandine	Fluorite	Ankerite	Epidote	Almandine is the 51th
Andesine	Alunite	Lepidolite	Illite	Andesine is the 12th
Ankerite	Gypsum	Orthoclase	Microcline	Ankerite is the 31th
Anorthite	Aluminum	Lepidolite	**Anorthite**	
Augite	Apatite	Olivine	Fluorite	Augite is 5th
Biotite	Aluminum	Microcline	Orthoclase	Biotite is the 33th
Bytownite	Labradorite	Andesine	Quartz	Bytownite is the 5th
Calcite	**Calcite**	Glauconite	Bassanite	
Chalcopyrite	Epidote	Ankerite	Fluorite	Chalcopyrite is the 32th
Diopside	Olivine	Biotite	Apatite	Diopside is 8th
Dolomite	**Dolomite**	Muscovite	Phlogopite	
Gypsum	**Gypsum**	Orthoclase	Cristobalite	
Hematite	Maghemite	Arsenopyrite	**Hematite**	
Ilmenite	**Ilmenite**	Chromite	Pyrite	
Labradorite	Alunite	Lepidolite	Illite	Labradorite is the 6th
Magnetite	Ankerite	Glauconite	Fluorite	Magnetite is the 65th
Microcline	Andesine	Aluminum	Labradorite	Microcline is 10th
Muscovite	Bytownite	Labradorite	Anorthite	Muscovite is the 15th
Olivine	Enstatite	Andalusite	Biotite	Olivine is the 4th
Phlogopite	Carnallite	Halite	Natron	Phlogopite is the 29th
Quartz	**Quartz**	Andesine	Beryl	
Talc	Phlogopite	Muscovite	Illite	Talc is 4th

Table 2: the three closest identified minerals obtained using the searching script applied on the validation set of minerals. The last column shows the rank of the sought mineral when it was not identified in the three closest minerals.

3. Discussion

The calibration step yielded very high R^2 correlation coefficients (0.97 for Z_{eff} model and 0.98 for ρ_e model) , in spite of two outliers. Titanium bar in figure 4 and 8% NaI in figure 5 do not perfectly fit: considering similar samples perform very well (another pure metal bar and other solutes), it is difficult to explain why these two outliers appear. However, despite their presence, the calibration is adequately performed.

The stoichiometric method validation estimated the effective atomic number Z_{eff} with less than 10% difference compared to theoretical value: out of a total of 23 minerals, 17 have less than 5% difference and, conversely, the largest deviations are for magnetite, ankerite, ilmenite, olivine, phlogopite and hematite in ascending order (table 1).

Bourque et al. (2014) obtained a smaller error, but in this study 10% is acceptable considering the samples we investigated, denser and more complex than human tissues; moreover, the final goal is the mineral identification among those of a chosen database, which is influenced by several factors and not only by the percentage error.

Figure 6 shows the iterative reweighted least squares trendline (red line) of minerals theoretical versus measured Z_{eff} perfectly matches with the least squares trendline (black line) and the theoretical trendline (dashed line, slope = 1); comparing the slopes, we observe our measurements underestimates the values.

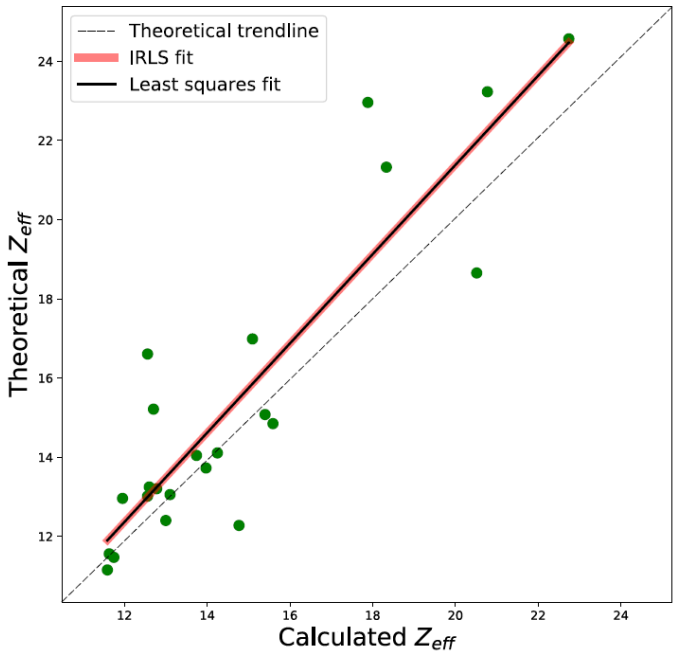

Figure 6: cross plot of theoretical versus measured Z_{eff} of minerals, using stoichiometric method.

The results for electron density ρ_e characterization are similar: 16 minerals have a difference between the measured and the theoretical values of less than 10%, of which 14 of them less than 5%, and the largest difference occurs for hematite, biotite, ankerite, chalcopyrite, almandine, phlogopite and magnetite in ascending order (table 1).

Figure 7 shows that iterative reweighted least squares trendline (red line) of minerals theoretical versus measured ρ_e involves a clear improvement of the fit compared to the least square method (black line), perfectly matching with the theoretical dashed line (slope = 1); nevertheless most outliers present underestimated values.

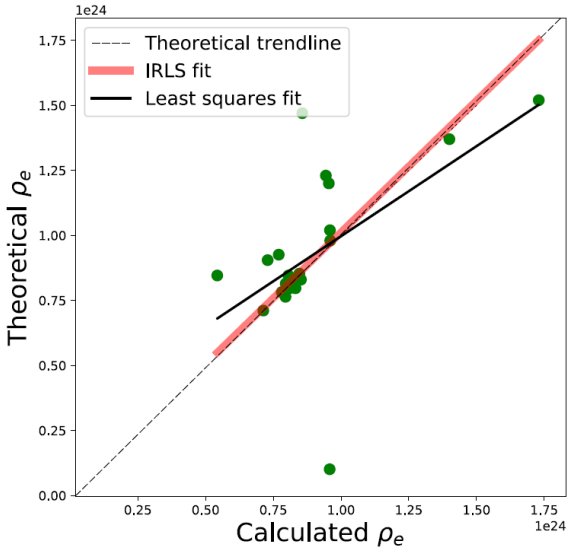

Figure 7: cross plot of theoretical versus measured ρ_e of minerals, using stoichiometric method.

The identification routine allowed to correctly pinpoint 7 minerals, including very common ones, i.e., albite, quartz and calcite (table 2). An interesting example is hematite: its identification is well performed, although its properties values present an high percentage error. Considering Z_{eff} and ρ_e distribution of the 69-mineral library (figure 8), we observe the majority is situated in a cluster of the graph having small Z_{eff} and ρ_e instead, common minerals with high Z_{eff} and ρ_e are less frequent. Thus, we successfully identified hematite even though its validation performance is weak because the Euclidean distance to its closest neighbour is larger than others (figure 8).

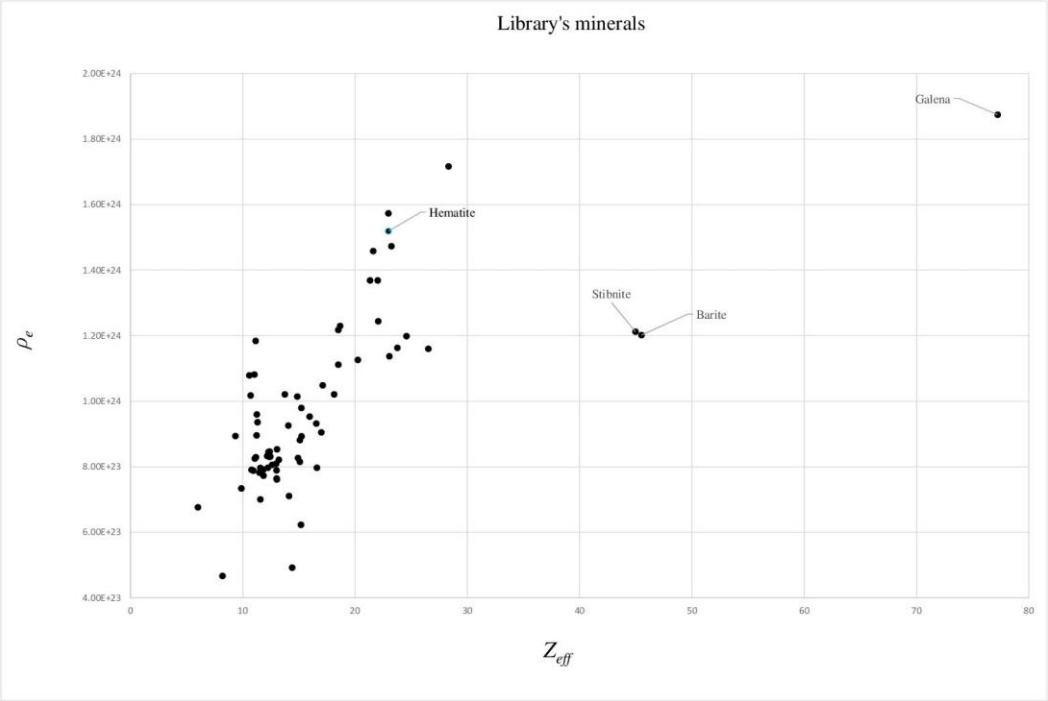

Figure 8: cross plot of Z_{eff} versus ρ_e of minerals chosen to develop the Python dictionary.

Several reasons could explain why some mineral samples have a wide difference between theoretical and measured values. First, because natural minerals contain impurities that are unknown in this experiment, it is likely the Z_{eff} and ρ_e calculated using equations 1 and 2 and theoretical mineral compositions are not reflecting the actual composition of the minerals used for both the calibration and the validation.

The second reason, similar to the first one, is that some minerals can easily interchange cations within their lattice, yet their precise elemental composition is rather impossible to obtain without specific analysis. Nine validation minerals fall under this case, explaining the poor identification obtained for phyllosilicates, such phlogopite, muscovite and biotite, and others such as ankerite (table 1). However, chalcopyrite, hematite, ilmenite and magnetite, in spite of their chemical formula not allowing for lattice cation substitutions, also have large differences with theoretical results for Z_{eff}, ρ_e or both properties: these minerals are the densest ones and, among the validation samples, it is remarkable that their values are mainly underestimated, according to iterative least squares trend. The performance of the stoichiometric protocol, previously developed for medical physics and human tissues, could be weaker for dense samples. It is possible that the exposure time with our medical CT is too low for having an accurate measurement of μ. Figure 9 shows the cross plot of minerals μ at low and high energy and the relative error bars having 95% confidence level: it is calculated following (Hazra et al., 2017):

$$x \pm Z\frac{s}{\sqrt{n}}$$

Where x is our measurement, Z is the value for determining confidence interval (here Z = 1.96), s is the standard deviation and n is the number of observations.

In order to avoid the overlapping, only some samples are illustrated but all of them present the same characteristic: horizontal error bar, related to low energy, is larger than the vertical one. This is true for minerals having large or small confidence intervals, so, probably, the need for improving the signal-to-noise ratio is stronger for lower voltage acquisitions (Gordic et al., 2014).

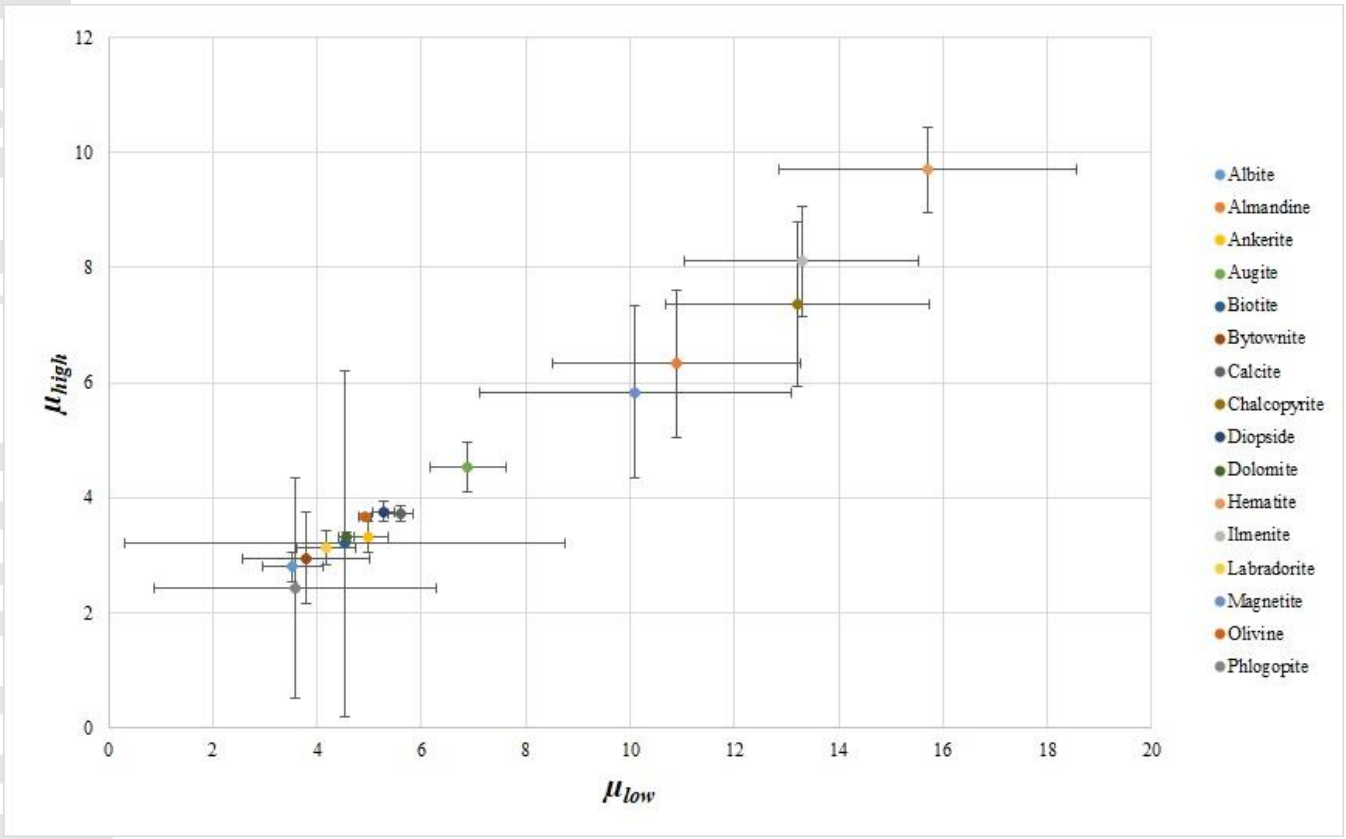

Figure 9: cross plot of minerals μ at low and high energy and the relative error bars having 95% confidence level.

The third possible reason is this stoichiometric method is not so well suited for dense samples; indeed, Bourque et al. used 140 keV as high energy, but the materials they aimed to characterize have smaller values of Z_{eff} and ρ_e than those investigated here. However, this explanation does not hold a close examination of our results because some dense minerals such as hematite and ilmenite (Z_{eff} = 22.96 and 21.3 respectively) are correctly identified (table 2). Our probable explanation is the answer resides in a combination of the above-mentioned factors: some samples have an underestimation for Z_{eff} and an overestimation for ρ_e and inversely, bringing the minerals in a value range favourable to their identification. Indeed, having a small relative difference between theoretical and measured values is not always sufficient to correctly identify the objects using the shortest Euclidean distance.

A possible improvement of this stoichiometric method could reside in increasing the exposure time or to acquire repeated scans in order to improve the signal-to-noise ratio (e.g., Larmagnat S. et al. (2019)), especially when very dense minerals, reducing the number of photons reaching the detectors, are present.

While the list of existing minerals totals more than 4000, our *ad hoc* library was limited to the 69 most common ones; however, in the most of the cases, some basic knowledge of natural samples such a rock would considerably shorten the list of potential minerals, hence improving the rate of correct classification. If the list of dense potential minerals remains limited to one or two, the method will likely be able to provide a correct identification.

Therefore, despite some drawbacks, stoichiometric method is a suitable option for the characterization of important and common minerals for geological field (quartz, calcite, dolomite) that are not distinguishable using single energy imaging method having very similar density values. Because CT-scanning rock and sediment cores is fast and non-destructive, this method is laying the foundation for an easy access to mineralogical information on geological samples.

4. Conclusion

Stoichiometric calibration is a methodology previously elaborated for medical purposes aiming to characterize the human tissues while removing the need for the knowledge of the incident X-ray energy spectra.

This work tested for the first time this technique on geological specimens, materials of greater density than the formerly studied biological samples. Two different calibrations were performed to characterize the effective atomic number and the electron density using 6 natural minerals, 2 metal bars and 11 saline solutions at different concentrations. Then, the calibration was validated with a set of 23 natural mineral samples selected to ensure they cover a wide range property values. Finally, an *ad hoc* routine search the minerals closest to the calculated Z_{eff} and ρ_e values and provides a list of decreasing possibilities.

We showed this stoichiometric dual-energy CT method is easy to implement and well suited to identify the most common minerals.

5. Data availability statement

All the data about calibration materials, measured linear attenuation coefficients μ of minerals and the Python scripts used for their identification are available at the Dataverse repository:

https://dataverse.scholarsportal.info/privateurl.xhtml?token=825cef86-ac16-46ad-9e9f-c3c0604f438b

Acknowledgements

This research was funded by *Fonds de recherche du Québec – Nature et technologies*. We would like to thank the colleagues Mathieu Des Roches, Philippe Latellier et Louis-Frederic Daigle of the *Institut national de la recherche scientifique* for their support and advice during the analysis carried out in this project.

References

Alvarez, R. E., Makovski, A. (1976). "Energy-selective Reconstructions in X-ray Computerized Tomography." Phys. Med. Biol. **21**: 733-744.
Alves, H., Lima I., de Assis J.T., Neves A.A., Lopes R.T. (2015). "Mineralogy evaluation and segmentation using dual-energy microtomography." X-Ray Spectrom. **44**: 99-104.
Azevedo, S. G., Martz H.E, Aufderheide M.B., Brown W.D., Champley K.M., Kallman J.S., Rberson G.P., Schneberk D., Seetho I.M. (2016). "System-Independent Characterization of Materials Using Dual-Energy Computed Tomography." IEEE TRANSACTIONS ON NUCLEAR SCIENCE **63**: 341-350.
Bazalova, M., Carrier J.-F., Beaulieu L., Verhaegen F. (2008). "Tissue segmentation in Monte Carlo treatment planning: a simulation study using dual-energy CT images." Radiotherapy and Oncology **86**: 93-98.
Boespflug, X., Long B.F.N., Occhietti S. (1995). "CAT-scan in marine stratigraphy: a quantitative approach." Marine Geology **122**: 281-301.
Bonnin, A., Duvauchelle P., Kaftandjian V., Ponard P. (2014). "Concept of effective atomic number and effective mass density in dual-energy X-ray computed tomography." Nuclear Instruments and Methods in Physics Research B **318**: 223-231.
Bourque, A. E., Carrier J.-F., Bouchard H. (2014). "A stoichiometric calibration method for dual energy computed tomography." Phys. Med. Biol. **59**: 2059-2088.
Brunelle, C. B., Des Roches M., Daigle L-F., Francus P., Long B., Després P. (2016). Combining CT scan and particle imaging techniques: applications in geosciences. The 4th International Conference on Image Formation in X-Ray Computed Tomography. Bamberg, Germany**:** 225-228.
Bushberg, J. T., Seibert, J.A., Leidholdt, E.M., Boone, J.M. (2012). The essential physics of medical imaging, LWW.
Cnudde, V., Boone M.N. (2013). "High-resolution X-ray computed tomography in geosciences: A review of the current technology and applications." Earth-Science Reviews **123**: 1-17.
Coenen, J. C. G., Maas J. (1994). Material classification by dual-energy computerized x-ray tomography. International symposium on computerized tomography for industrial applications**:** 120–127.
Coolens, C., Childs P.J. (2003). "Calibration of CT Hounsfield units for radiotherapy treatment planning of patients with metallic hip prostheses: the use of the extended CT-scale." Phys. Med. Biol. **48**: 1591-1603.
Duchesne, M. J., Moore F., Long B.F., Labrie J. (2009). "A rapid method for converting medical Computed Tomography scanner topogram attenuation scale to Hounsfield Unit scale and to obtain relative density values." Engineering Geology **103**: 100-105.
Duliu, O. G., Rizescu C.T., Ricman C. (2003). "Dual energy gamma-ray axial computer tomography investigation of some metamorphic and sedimentary rocks." N. Jb. Geol. Paläont. Abh. **228**: 343-362.
Gordic, S., Desbiolles, L., Stolzmann, P., Gantner, L., Leschka, S., Husarik, D.B., Alkadhi, H. (2014). "Advanced modelled iterative reconstruction for abdominal CT: Qualitative and quantitative evaluation." Clinical Radiology **69**: e497-e504.
Hazra, A. (2017). "Using the confidence interval confidently." J Thorac Dis. **10**: 4125-4130.
Iovea, M., Neagu M., Duliu O.G., Oaie G., Ricman C., Mateiasi G. (2006). Dual-Energy Computer Tomography and Digital Radiography Investigation of Organic and Inorganic Materials. ECNDT. **Poster 44**.

Iovea, M., Oaie G., Ricman C., Mateiasi G., Neagu M., Szobotka S., Duliu O.G. (2009). "Dual-energy X-ray computer axial tomography and digital radiography investigation of cores and other objects of geological interest." Engineering Geology **103**: 119-126.
Jackson, D. F., Hawkes D.J. (1981). "X-ray attenuation coefficient of elements and mixtures." Phys. Rep. **70**: 169-233.
Jussiani, E. I., Appoloni, C. R. (2015). "Effective atomic number and density determination of rocks by X-ray microtomography." Micron **70**: 1-6.
Landry, G., Seco J., Gaudreault M., Verhaegen F. (2013). "Deriving effective atomic numbers from DECT based on a parameterization of the ratio of high and low linear attenuation coefficients." Phys. Med. Biol. **58**: 6851-6866.
Larmagnat S., D. R. M., Faigle L-F., Francus P., Lavoie D., Raymond J., Malo M., Aubiès-Trouilh A. (2019). "Continuous porosity characterization: Metric-scale intervals in heterogeneous sedimentary rocks using medical CT-scanner." Marine and Petroleum Geology **109**: 361-380.
Manohara, S. R., Hanagodimath S.M., Thind K.S., Gerward L. (2008). "On the effective atomic number and electron density: a comprehensive set of formulas for all types of materials and energies above 1 keV." Nuclear Instruments and Methods in Physics Research (section B) **266**: 3906-3912.
Mees, F., Swennen R., Van Geet M., Jacobs P. (2003). "Applications of X-ray computed tomography in the geosciences." Geological Society **215**: 1-6.
Paziresh, M., Kingston A.M., Latham S.J., Fullagar W.K., Myers G.M. (2016). "Tomography of atomic number and density of materials using dual-energy imaging and the Alvarez and Macovski attenuation model." Journal of applied Physics **119**.
Remeysen, K., Swennen R. (2008). "Application of microfocus computed tomography in carbonate reservoir characterization: Possibilities and limitations." Marine and Petroleum Geology **25**: 486-499.
Remysen, K., Swennen R. (2006). "Beam hardening artifact reduction in microfocus computed tomography for improved quantitative coal characterization." International Journal of Coal Geology **67**: 101-111.
Rezvan, R. H., Chatterjee, S., Akondi, V., Pratik, K., Sanjay, T. (2011). "X-ray attenuation coefficient of mixtures: Inputs for dual-energy CT." Med. Phys. **38**: 5270-5279.
Rizescu, C., Beşliu C., Jipa A. (2001). "Determination of local density and effective atomic number by the dual-energy computerized tomography method with the ^{192}Ir radioisotope." Nuclear Instruments and Methods in Physics Research (section A) **465**: 584-599.
Rutherford, R. A., Pullan B.R., Isherwood (1976). "Measurement of Effective Atomic Number and Electron Density Using an EMI Scanner." Neuroradiology **11**: 15-21.
Schneider, U., Pedroni E., Lomax A. (1996). "The calibration of CT Hounsfield units for radiotherapy treatment planning " Phys. Med. Biol. **41**: 111-124.
Siddiqui, S., Khamees, A. A. (2004). Dual-Energy CT-Scanning Applications in Rock Characterization. SPE Annual Technical Conference and Exhibition. Houston, Texas.
Spiers, W. F. (1946). "Effective Atomic Number and Energy Absorption in Tissues." The General Infirmary, Leeds **19**(218): 52-63.
Stamm, D. (1974). "Calibration and quality control materials." Z. Klin. Chem. Klin. Biochem. **4**: 137-145.
Torikoshi, M., Tsunoo T., Sasaki M., Endo M., Noda Y., Ohno Y., Kohno T., Hyodo K., Uesugi K., Yagi N. (2003). "Electron density measurement with dual-energy x-ray CT using synchrotron radiation." Phys. Med. Biol. **48**: 673–685.
Tsunoo, T., Torikoshi M., Ohno Y., Endo M., Natsuhori M., Kakizaki T., Yamada N., Ito N., Yagi N., Uesugi K. (2004). "Measurement of electron density and effective atomic number using dual-energy x-ray CT." IEEE Symposium Conference Record Nuclear Science 2004.
Van Geet, M., Swennen R., Wevers M. (2000). "Quantitative analysis of reservoir rocks by microfocus X-ray computerised tomography." Sedimentary Geology **132**: 25-36.

Victor, R. A., Prodanovic, M., Torres-Veredin, C. (2017). "Monte Carlo Approach for Estimating Density and Atomic Number From Dual-Energy Computed Tomography Images of Carbonate Rocks." JGR Solid Earth **122**: 9804-9824.
Vinegar, H. J., Wellington S.L. (1987). "Tomographic imaging of three-phase flowexperiments." Review of Scientific Instruments **58**: 96-107.
Watanabe, Y. (1999). "Derivation of linear attenuation coefficients from CT numbers for low-energy photons." Phys. Med. Biol. **44**: 2201-2211.
Youn, E., Jeong M.K. (2009). "Class dependent feature scaling method using naive Bayes classifierfor text datamining." Pattern Recognition Letters **30**: 477-485.